International Journal of Minerals, Metallurgy and Materials
Volume 29, Number 1, January 2022, Page 144
https://doi.org/10.1007/s12613-020-2171-4

Process–structure–property relationship for plasma-sprayed iron-based amorphous/crystalline composite coatings

Abhishek Pathak[1)], *Biswajyoti Mukherjee*[2)], *Krishna Kant Pandey*[2)], *Aminul Islam*[2)], *Pavan Bijalwan*[1)], *Monojit Dutta*[1)], *Atanu Banerjee*[1)], *and Anup Kumar Keshri*[2),✉]

1) Research and Development Unit, Tata Steel, Jamshedpur 831001, India
2) Plasma Spray Coating Laboratory, Metallurgical and Materials Engineering, Indian Institute of Technology Patna, Bihta 801106, India
(Received: 1 July 2020; revised: 14 August 2020; accepted: 25 August 2020)

Abstract: This study explores the fabrication of Fe-based amorphous/crystalline coating by air plasma spraying and its dependency on the coating parameters (plasma power, primary gas flow rate, powder feed rate, and stand-off distance). X-ray diffraction of the coatings deposited at optimized spray parameters showed the presence of amorphous/crystalline phase. Coatings deposited at a lower plasma power and highest gas flow rate exhibited better density, hardness, and wear resistance. All coatings demonstrated equally good resistance against the corrosive environment (3.5wt% NaCl solution). Mechanical, wear, and tribological studies indicated that a single process parameter optimization cannot provide good coating performance; instead, all process parameters have a unique role in defining better properties for the coating by controlling the in-flight particle temperature and velocity profile, followed by the cooling pattern of molten droplet before impingement on the substrate.

Keywords: Fe-based alloys; amorphous alloys; plasma spray coating; mechanical; corrosion and wear

1. Introduction

Metallic glasses are a promising material for industrial applications due to their high hardness, strength, and excellent anti-corrosion and anti-wear properties [1–3]. Among the various systems of metallic glasses developed, iron (Fe)-based metallic glasses have attracted special attention owing to their pseudo-amorphous phase [4–6]. This unique feature provides much higher mechanical strength, corrosion resistance, and wear resistance properties to the Fe-based metallic glasses compared with their traditional crystalline counterparts [5–6]. In addition to these features, the ease of availability and lower cost associated with Fe provides the potential to fulfill the demand of current industries. As a result, Fe-based metallic glasses, to some extent, have become industry favorites for structural applications operating in mild to aggressive environments.

However, like every other material on the planet, this material also possesses a drawback. Most studies on Fe-based bulk metallic glass (BMG) dealt with complete amorphous phase, and the inherent brittleness associated with this phase was mostly ignored [7]. A detail that is worth mentioning here is that the complete amorphous phase imparts poor fracture toughness to this metallic glass, thereby preventing its widespread applications as a structural material. In this regard, the coexistence of amorphous and crystalline phases in Fe-based metallic glasses has not only proven to be a hardness energizer but has also improved the overall toughness of the material. Li *et al*. [8] demonstrated that arc-melted Fe-based metallic glass with amorphous/crystalline phase increases the fracture toughness of the BMG. Kumar *et al*. [9] reported that the Fe-based metallic coating consisting of both amorphous and crystalline phases showed enhanced hardness and wear resistance properties. The higher wear resistance was ascribed to the decrease in the brittleness of the coating, which translates to increased toughness of the coating. Moreover, the composite (amorphous and crystalline) phase is already being used as structural materials in boilers, turbines, and auto parts [9].

Although many protocols such as mechanical alloying, arc melting, laser cladding, and selective laser melting can be used to fabricate Fe-based metallic glasses, the varying degree of limitations associated with these protocols prevents most of them from gaining industrial status [8,10–15]. In this regard, due to its widespread usage and ease of fabrication, thermal spraying has been widely regarded as a benign industrial technique to fabricate metallic glass coatings [16–18]. The unmatched rate of cooling (~10^6–10^7 K/s) associated with this technique also helps retain the amorphous phase in the coating [19]. Several studies in recent years have successfully retained the complete amorphous phase in coating after thermal spraying of amorphous starting powders.

✉ Corresponding author: Anup Kumar Keshri E-mail: anup@iitp.ac.in

Guo *et al.* [20] fabricated Fe-based amorphous $Fe_{49.7}Cr_{18}Mn_{1.9}Mo_{7.4}W_{1.6}B_{15.2}C_{3.8}Si_{2.4}$ coating over mild steel substrate by using high-velocity air fuel (HVAF) and high-velocity oxygen fuel (HVOF) processes. X-ray diffraction (XRD) study showed that the coating completely retained its amorphous phase after spraying. Similar results were obtained in the studies conducted by Koga *et al.*, where the amorphous $Fe_{60}Cr_8Nb_8B_{24}$ alloy almost retained its phase in the coating fabricated by HVOF [21]. In both studies, the complete transformation of amorphous phase was prevented due to the rapid quenching involved in HVOF/HVAF, which prevented the crystallization of disordered amorphous powders.

However, as discussed earlier, even though thermal spraying helps retain the complete amorphous phase, the formation of amorphous/crystalline is expected to further enhance the properties of the Fe-based metallic coating. Zhang *et al.* [22] attempted to deposit Fe-based amorphous powders ($Fe_{45}Cr_{16}Mo_{16}C_{18}B_5$) over carbon steel by using atmospheric plasma spraying at different plasma powers (25, 30, 35, and 40 kW). They observed that the coating fabricated using 40 kW demonstrated amorphous/crystalline phase. Kumar *et al.* [9] studied the optimization of amorphous/crystalline phase of amorphous Fe–2.5Cr–6.7Si–2.5B–0.7C (wt%) powder at various plasma powers (20, 25, 30, and 35 kW). All the coatings displayed amorphous/crystalline phase as the crystalline content increased from 14.0% to 20.0% as the plasma power increased from 20 to 35 kW. This dual phase enhanced the mechanical and wear resistance properties of the Fe metallic glass coating. However, the optimization in both studies involved only the variation of plasma power and overlooked the influence of other three key plasma process parameters, namely, primary gas flow rate, powder feed rate, and stand-off distance. All four key plasma process parameters need to be considered together to approach a conclusive result. That being said, an interesting detail to note is that not even a single study explored the complete optimization of Fe-based metallic glass.

Therefore, this study attempts to develop a composite (amorphous/crystalline) coating through optimization of the plasma spraying parameters from a very lean Fe-based alloy composition ($Fe_{92.6}C_{3.5}P_{1.4}Si_2Mn_{0.5}$). This alloy is obtained as a residue material with pig iron as a regular output from the blast furnace in an integrated steel plant. To reuse this residue cost effectively, this alloy was synthesized with minimum modifications in the compositions. Four key plasma process parameters, namely, plasma power, primary gas flow rate, powder feed rate, and stand-off distance, were varied simultaneously to study their effect on the amorphization/crystallization and structure of all the coatings. In addition, the mechanical, corrosion, and wear properties were studied, and correlations were drawn with the process parameters.

2. Experimental

2.1. Powder details

Commercially available high-phosphorus pig iron ingots were converted to Fe-based powder ($Fe_{92.6}C_{3.5}P_{1.4}Si_2Mn_{0.5}$) (all compositions in wt%, average particle size: 30–80 μm) at the manufacturing unit of Innomet Powders, India. The powder is mostly crystalline in nature (see Section 3.1) and is prepared using water atomization technique.

2.2. Assessing various plasma spray parameters

In this work, the four key air plasma spray (APS) parameters—plasma power (P), gas flow rate (G), powder feed rate (F), and stand-off distance (S)—were varied to synthesize coatings. Varying these parameters is believed to alter the temperature and velocity of the in-flight molten particles, which will have a significant impact on the coating properties. Thirty-six experiments (Table S1) were conducted based on several combinations of P, G, F, and S. The coatings were deposited using a 9 MB plasma gun and accessories (Oerlikon Metco, Switzerland). Three sets of plasma power (P_1 = 25 kW, P_2 = 30 kW, and P_3 = 35 kW) and gas flow rate (G_1 = 2.80 m^3/h, G_2 = 3.36 m^3/h, and G_3 = 3.92 m^3/h), and two sets of powder feed rate (F_1 = 15 g/min and F_2 = 30 g/min) and stand-off distances (S_1 = 75 mm and S_2 = 100 mm) were varied to perform the experiments. Coatings were deposited over a grit-blasted plain carbon steel substrate (dimensions: 100 mm × 20 mm × 3 mm). Substrates were preheated at 200°C prior to the deposition of the coating. The substrate temperature was monitored using an optical pyrometer (HTC Instruments, Model IRX 69, Mumbai, India). Substrate preheating contributes in minimizing the thermal mismatch with the molten particle, hence reducing the chance of coating delamination [23].

The aim of this work is the thorough optimization of process parameters to achieve the best combination of mechanical, wear-resisting, and corrosion-resisting properties. Thus, the thermal and kinetic history of the molten in-flight powder was also studied. The thermal and kinetic values for each process were constantly monitored using an in-flight particle diagnostic sensor (Accuraspray; Tecnar Automation Ltée, QC, Canada). Details of the data acquisition of the in-flight particle diagnostic sensor were discussed in our previous study [24].

2.3. Characterization analysis for powder and coating

A helium gas pycnometer (Ultrapyc, Model 1200e, Quantachrome Instruments, USA) was used to measure the densities of the coatings. For this purpose, coatings of the Fe-based feedstock were made on a plane carbon steel substrate (without grit blasting). Coatings on the non-grit-blasted substrates led to the coatings to detach from the substrates, which is mainly attributed to two reasons: (i) a high thermal mismatch between the substrate and the coating, and (ii) lower adhesion of the coatings with the substrate due to lack of an interlocking bond between them. Free standing coatings were filled in a 0.25 cm^3 cell, and the outlet gas pressure was fixed at 34 kPa. Phase analysis of the synthesized coatings and the powder was performed using XRD (TTRAX III, Rigaku, Japan) of Cu K_α radiation of 0.154 nm wavelength. All spectra were captured at a scanning rate of 2°/min between 30° and

90° (2θ). High-resolution transmission electron microscope (HR-TEM) (FEI Tecnai, USA) operating at 200 kV was used for imaging and obtaining the selected area electron diffraction (SAED) of the powder. The morphology of the commercially obtained Fe-based powders and the cross section of all the coatings were obtained using a field emission scanning electron microscope (FESEM, Zeiss, Sigma HD, Germany) at an operating voltage of 15 kV. Thermal analysis of the powder and free-standing coatings was performed using a differential scanning calorimeter (DSC) (NETZSCH STA F449, Germany) at 10°C/min in a temperature range of 30–700°C under nitrogen atmosphere.

2.4. Mechanical-, wear-, and corrosion-property analysis

The mechanical properties (hardness and elastic modulus) of the optimized coatings were measured using an instrumented micro-indenter (Microtest, MTR 3, Spain) at a load of 3 N and holding time of 5 s. At least five indents were made for each coating. Wear tests were carried out using a ball-on disk tribometer (Ducom, TR-20LE-CHM800, India) at 250 r/min and at 20 N normal load with a fixed sample and rotating alumina (Al_2O_3) ball. All wear tests were conducted for 3600 s without any interruption. Electrochemical measurements were performed to evaluate the corrosion resistance performance of the coating. Standard 3.5wt% NaCl aqueous solution was used as the standard corrosion media. The open circuit potential (OCP) values of the coatings were recorded to obtain a stable potential before dynamic polarization measurements. The corrosion potential (E_{corr}) and corrosion current (I_{corr}) values were obtained by extrapolating the anodic and cathodic curves using the Tafel method. Corrosion rate was evaluated using Gamry Echem Analyst software, which uses Faraday law to calculate the corrosion rate.

3. Results and discussion

3.1. Characterization of Fe-based powder

Fig. 1(a) shows the low-magnification FESEM images of the Fe-based powder depicting the irregular morphology, which is a typical of water-atomized powders, and the inset shows the corresponding high-magnification image of the powder. Fig. 1(b) shows the average particle size distribution of the Fe-based powders. The average particle size distribution of the powders was measured by considering more than 100 particles. The longest diagonal was considered while measuring the particle size. The average powder size of the Fe-based powders is (62.0 ± 12.0) μm (Fig. 1(b)). The wide range of particle sizes is expected to be beneficial because smaller particles can melt easily and impart higher mechanical properties, whereas coarser particles give rise to amorphous phase, thereby increasing the corrosion resistance of the coating. In addition, even though the powders are irregularly

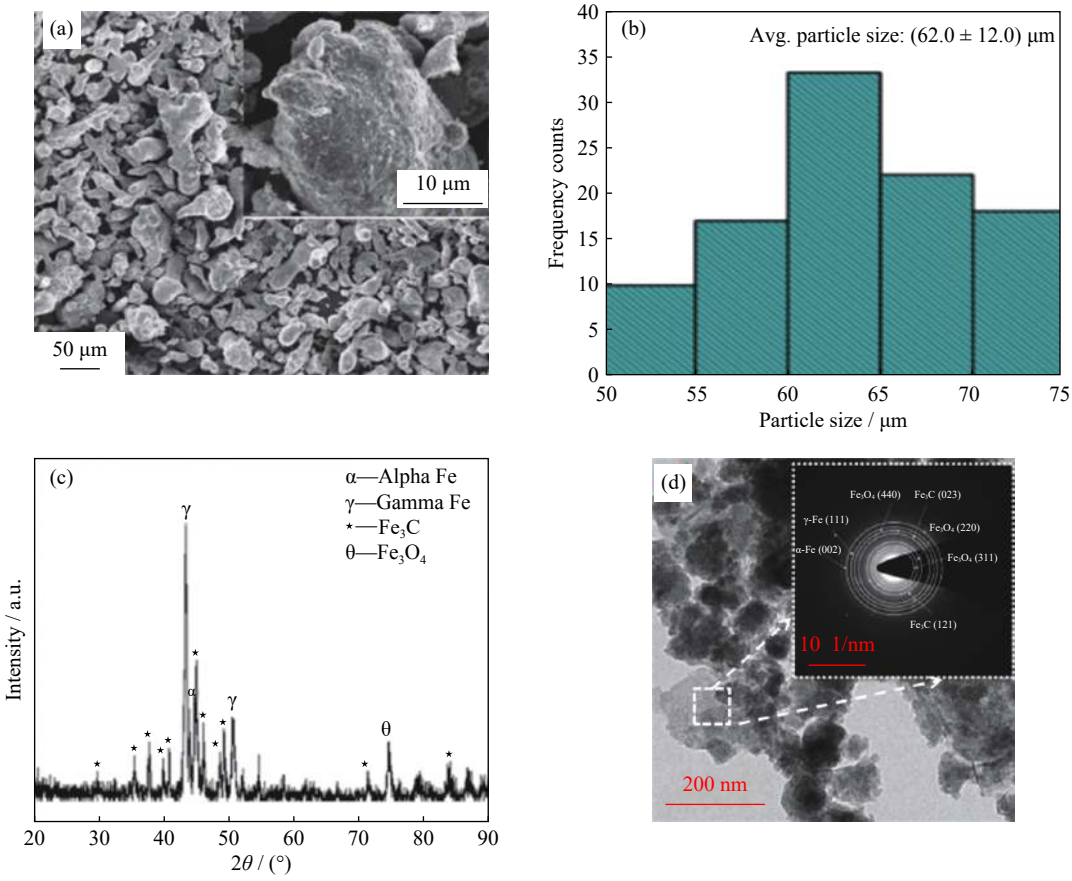

Fig. 1. (a) FESEM image of the commercially obtained Fe-based powder, and the inset shows the high-magnification image of the powder; (b) powder size distribution (Avg. means average); (c) XRD pattern of the powder; (d) HR-TEM of the powder, and the inset is the SAED from the area shown in (d).

shaped, a larger size could assist in smooth flowability of the powders. The flowability of powder in the nozzle is an important factor for fabricating uniform and good-quality coatings. The ease of powder flow through the powder feeder (5MPE, Oerlikon Metco, Switzerland) was estimated by passing the Fe powder through the feeder hose. The deviation of the amount of the powder weighed (per minute) with the instrumented or theoretical feed rate provided the uniformity of the flow. Less deviation corresponded to more uniformity of the powder flow in the powder feeder. More details are included in Section S1.

Fig. 1(c) shows the XRD pattern of the Fe-based powder. The amorphous phase content of the powder was 21.75%, which shows that the starting powder is mostly crystalline in nature. The amorphous phase fraction was calculated from the ratio of the total area of the amorphous peak to the total area of all peaks [25]. The phase constituents were also evaluated using HR-TEM. Fig. 1(d) shows the HR-TEM image of the Fe-based powder. Selected area electron diffraction (SAED) along the entire area confirms the various phases that are present, which are also shown in XRD. DSC was performed to determine the crystallization temperature of the powder. Fig. S1 shows the DSC profile of the powder. A sharp exothermic peak can be observed at 520°C for the powder. This finding implies that heat is released at 520°C, which denotes the crystallization temperature (T_x) for the powder, depicting high thermal stability.

3.2. Optimization of plasma process parameters

The powder was plasma-sprayed over plain carbon steel substrate for the 36 different parameters. The in-flight particle temperature and velocity were recorded for every spraying parameter variation and are mentioned in Table S1. Fig. 2 displays the integrated process map showing the temperature and velocity distribution of in-flight powder particle at two different powder feed rates of 15 and 30 g/min, respectively. Fig. 2(a)–(b) shows the temperature and velocity of the particles at 75 mm stand-off distance, while Fig. 2(c)–(d) shows the temperature and velocity of the particles at 100 mm stand-off distance. The relative size of the legends in Fig. 2 is directly proportional to the plotted temperature and velocity values. Fig. 2(a) shows that for the same power and feed rate, the temperature decreases marginally with the increase in primary gas flow rate. In contrast, for the same power and primary gas flow rate, the temperature decreases marginally in most of the cases with the increase in feed rate, except for few parameters with highest power. As shown in the Table S1, the temperature of $P_3G_1F_1S_1$ is reported lower than that of $P_3G_1F_2S_1$ and the temperature of $P_3G_2F_1S_1$ is lower than that of $P_3G_2F_2S_1$, although the differ-

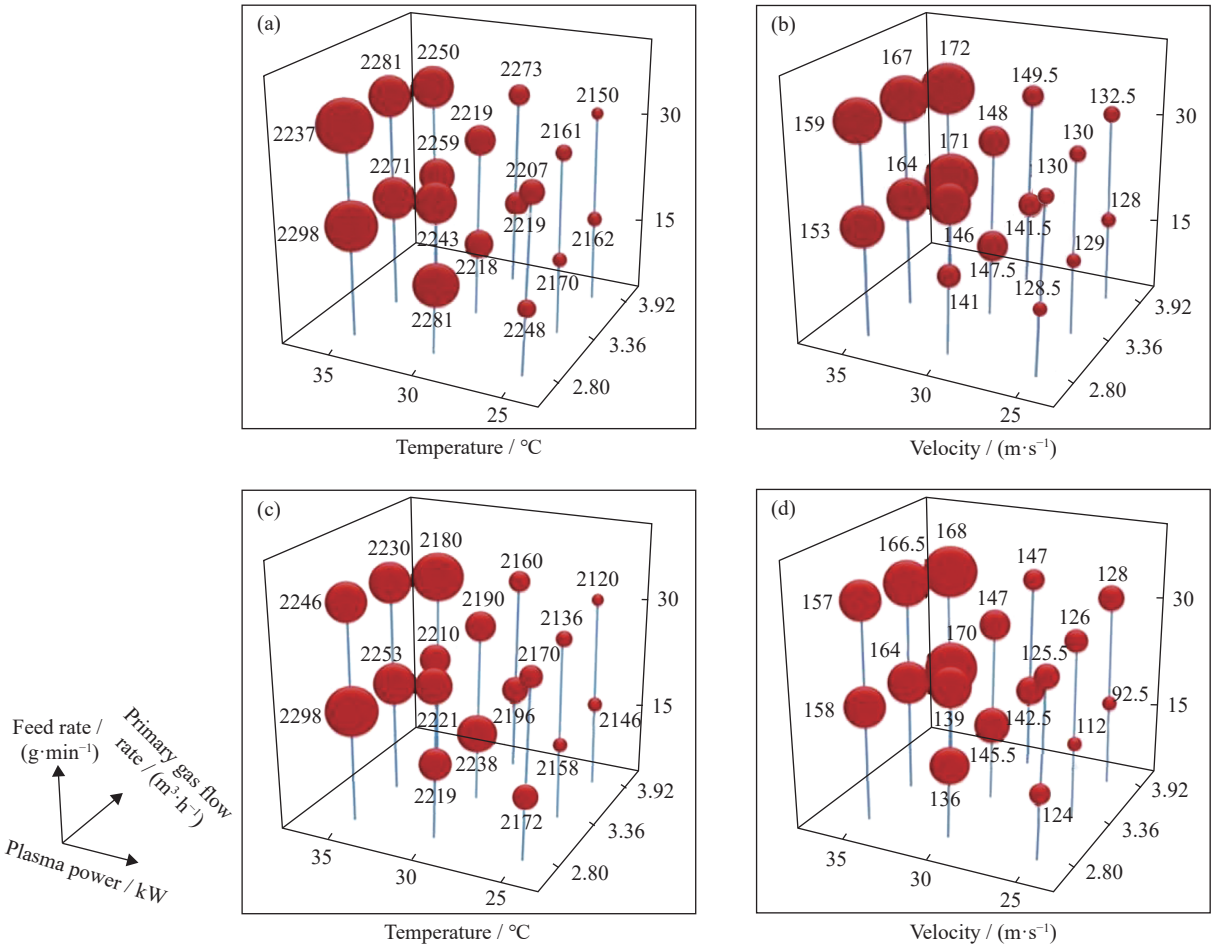

Fig. 2. Temperature (a, c) and velocity (b, d) distributions of in-flight powder particle at two different stand-off distances of 75 and 100 mm, respectively, in the plasma process.

ences were marginal. However, in the velocity profile (Fig. 2(b)), for the same power and feed rate, the velocity increases marginally or remains constant with the increase in primary gas flow rate, except with very little exemptions in the power (30 kW). However, for the same power and primary gas flow rate, the velocity increased minimally with the increase in the powder feed rate. In addition, both temperature and velocity increased with the increase in plasma power for all combinations. Therefore, collectively, for a stand-off distance of 75 mm, the highest temperature and velocity recorded throughout the entire series are 2327°C (P = 35 kW, G = 2.80 m^3/h, and F = 30 g/min) and 172 m/s (P = 35 kW, G = 3.92 m^3/h, and F = 30 g/min), respectively. However, when the stand-off distance was increased to 100 mm, discrepancies in the values of temperature and velocities were observed when compared with the values obtained using a lower stand-off distance (75 mm). The highest temperature and velocity in this case were 2298°C (P = 35 kW, G = 2.80 m^3/h, and F = 15 g/min) and 170 m/s (P = 35 kW, G = 3.92 m^3/h, and F = 15 g/min), respectively. Besides, the highest temperature and velocity are lower in data accumulated at a stand-off distance of 75 mm. The above results indicate that a conclusive parameter cannot be obtained by using plasma power alone but depends on the other three parameters as well.

On the basis of the above 36 values of temperature and velocities, five distinct parameters were chosen for temperature and five values for velocity on the basis of the highest, lowest, middle, and intermediate (i.e., between highest and middle values and between middle and lowest values) values obtained for each set of temperature and velocity, as shown in Table 1.

Table 1. 10 selected optimized parameters with respect to temperature and velocity values

Parameters	Temperature / °C	Parameters	Velocity / ($m \cdot s^{-1}$)
$P_3G_1F_2S_1$	2327	$P_3G_3F_2S_1$	172
$P_3G_3F_2S_1$	2259	$P_3G_1F_2S_1$	159
$P_2G_3F_1S_1$	2219	$P_2G_1F_2S_1$	146
$P_1G_2F_1S_1$	2170	$P_1G_2F_2S_1$	130
$P_1G_3F_2S_2$	2120	$P_1G_3F_1S_2$	92.5

Plasma-sprayed Fe coating was fabricated using the 10 parameters, as listed in Table 1. However, the coating obtained using plasma power P_3 = 35 kW melted during the plasma spraying process. This condition was consistent with all the coatings prepared using the highest power (35 kW). However, the remaining coatings showed no sign of melting. This melting of the P_3 batch coatings could be attributed to the very high temperature, which melts the powder and does not allow the powder to cool and solidify upon continuous plasma gun passes. Fig. S2(a) shows a digital image of the melted P_3 batch coating. The coating obtained using parameter $P_2G_3F_1S_1$ also showed signs of melting (Fig. S2(b)).

Therefore, all the coatings prepared with power P_3 and $P_2G_3F_1S_1$ were dropped and were not considered hereafter. Hence, the rest of the five best parameters—$P_1G_3F_2S_2$, $P_1G_2F_1S_1$, $P_1G_3F_1S_2$, $P_2G_1F_2S_1$, and $P_1G_2F_2S_1$—were chosen for fabrication of the optimized coating. Fig. 3 shows the cross-sectional SEM images of the coatings. All coatings demonstrated a uniform thickness of ~250 μm. Moreover, the coatings appeared to be well adhered to the substrate, thereby validating the satisfactory bonding between them. The density of these free-standing coatings was measured using a helium gas pycnometer.

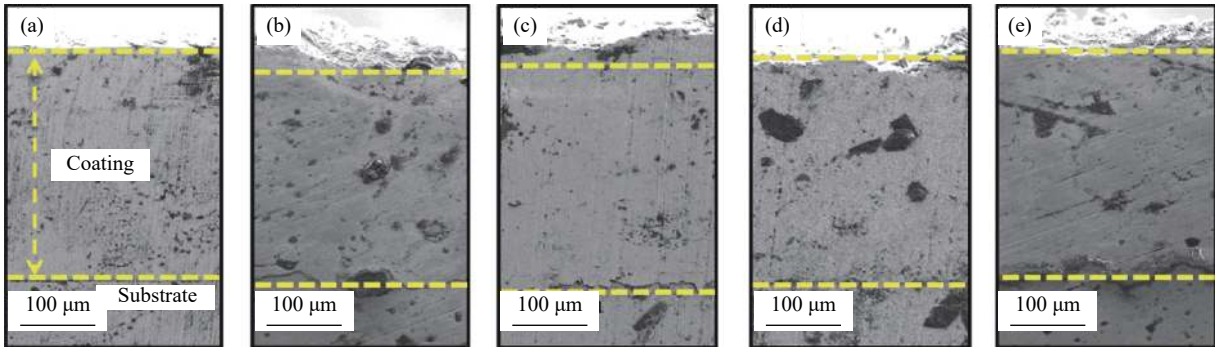

Fig. 3. Cross-sectional SEM images of (a) $P_1G_3F_2S_2$, (b) $P_1G_2F_1S_1$, (c) $P_1G_3F_1S_2$, (d) $P_2G_1F_2S_1$, and (e) $P_1G_2F_2S_1$.

Table 2 depicts the average relative densities of the free-standing coatings along with their standard deviation. As seen from Table 2, the coating synthesized at spray parameter $P_1G_3F_1S_2$ shows the highest average relative density (~98%), while $P_2G_1F_2S_1$ shows the lowest average relative density (94.3%). The minimum power combined with a suitable amount of in-flight time is assumed to be beneficial to the proper melting of the particles, which might have helped increase the density of the coating. As an example, an increase in the gas flow rate lessens the in-flight time of the molten splats and restricts their cooling during their way to substrate. Consequently, it facilitates the early deposition of the splats onto the substrate, resulting in improved density of

Table 2. Average relative densities of the coatings synthesized at optimized parameters

Parameters	Average relative density / %
$P_1G_3F_2S_2$	97.9 ± 0.3
$P_1G_2F_1S_1$	96.8 ± 0.6
$P_2G_1F_2S_1$	94.3 ± 0.7
$P_1G_3F_1S_2$	98.1 ± 0.4
$P_1G_2F_2S_1$	95.3 ± 0.8

the coatings. Prior studies also saw an increase in the density of the coatings with the increase in the gas flow rate in a plasma spray system [26–27]. A low powder feed rate also improves the density of coatings through better melting by providing ample time for powder–plume interaction [26].

3.3. Phase and thermal analysis of the optimized coatings

Fig. 4 shows the XRD pattern of all the five coatings fabricated using parameters of $P_1G_2F_1S_1$, $P_1G_3F_2S_2$, $P_2G_1F_2S_1$, $P_1G_2F_2S_1$, and $P_1G_3F_1S_2$. A mixture of α-Fe, Fe_3C, and Fe_3O_4 phase was observed in all the coatings. The characteristic semi-sharp peaks in the XRD denote that the coatings are not completely amorphous. However, the degree of amorphous phase increased in the coating compared with that in the powder. The presence of sharp peaks and broad halos in the XRD pattern signifies the existence of a mixture of crystalline and amorphous phase in the coating. The amorphous content is calculated and presented in Table 3.

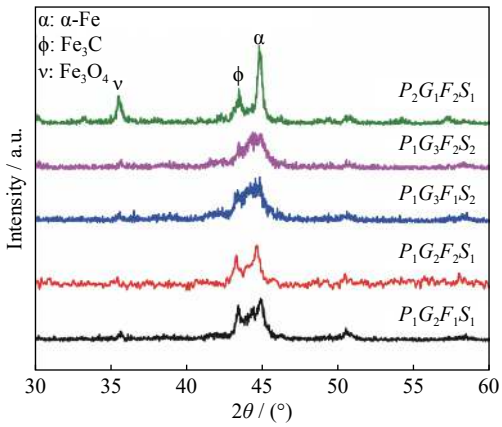

Fig. 4. XRD pattern of Fe-based coatings synthesized at different spray parameters.

Table 3. Amorphous content in all the fabricated coatings and the initial powder calculated using XRD

Parameters	Amorphous content / %
$P_1G_2F_1S_1$	42.68
$P_1G_2F_2S_1$	44.32
$P_1G_3F_1S_2$	50.72
$P_1G_3F_2S_2$	53.55
$P_2G_1F_2S_1$	33.85
Powder	21.75

The amorphous phase increases in all coatings when compared with that of the powder used for spraying. However, the amorphous content is lowest in the coating fabricated at higher power ($P_2G_1F_2S_1$). The coatings fabricated using parameter $P_1G_3F_2S_2$ shows the highest percentage of amorphous phase. Partial amorphization occurs in all coatings, as confirmed by the low-intensity XRD peaks. When the powder comes in contact with the plasma plume, the powder melts and amorphous-natured coatings begin to form due to the very high quenching rate involved in plasma spraying [17]. However, the high crystalline phase percentage at high temperature (P_2) could be attributed to the accumulation of heat at a higher power and simultaneously their oxidation at this high temperature, which could lead to the crystallization of the amorphous phase. Kumar *et al*. also observed a decrease in the amorphous content with the increase in plasma power [17]. Moreover, increasing the primary gas flow rate increases the amorphous content in the coatings. The increase in the primary gas trims the temperature and shortens the residence time of in-flight particles, providing a higher quenching rate for them and reducing the probability of oxidation. Another detail that is interesting to note is that among the five coatings, the coatings fabricated with stand-off distance S_2 = 100 mm resulted in a higher amorphous phase ($P_1G_3F_2S_2$: 53.55%; $P_1G_3F_1S_2$: 50.72%) compared with the coatings fabricated at S_1 = 75 mm. This condition occurred because a lower stand-off distance translates to lower residence time of the in-flight particles, which allows the feedstock to quench with abnormally high cooling rate. The quenching consequently tends to support the crystallization of the coatings and vice-versa.

To find the crystallization temperature and enthalpy of crystallization (ΔH), DSC was performed on all the five coatings (Fig. S3). A sharp exothermic peak can be observed at T = 518.98°C for the coating prepared using parameter $P_1G_3F_2S_2$. This finding implies that heat is released at T = 518.98°C, which denotes the crystallization temperature for the coating. Similarly, the crystallization temperature of the optimized coatings lies between 514.60 and 518.98°C. The ΔH of all the five coatings is presented in Table S3. As seen from Table S3, the coating prepared using the parameter set $P_1G_3F_1S_2$ shows relatively higher ΔH (12.12 kJ/g), while the coating prepared using the parameter set $P_2G_1F_2S_1$ shows the lowest ΔH (8.81 kJ/g).

3.4. Mechanical property evaluation

The micro-hardness values of the coatings were measured using the load versus displacement (L–D) curve obtained from micro-indentation technique. Fig. 5 shows the L–D curve for all the coatings. The average hardness and elastic modulus values are tabulated in Table 4. The coating prepared with parameter set $P_1G_3F_1S_2$ shows relatively higher hardness ((6.56 ± 0.97) GPa), while the coating prepared with parameter set $P_1G_3F_2S_2$ shows the highest elastic modulus ((89.65 ± 3.15) GPa). All the coatings fabricated at lowest power P_1, highest gas flow rate G_3, and high stand-off S_2 ($P_1G_3S_2$) display higher mechanical properties. However, upon careful examination, the combination $P_1G_3S_2$ gives slightly higher hardness for F_1, while F_2 yields the highest elastic modulus. An important detail to note is that, while not the highest, the coatings fabricated at parameter $P_2G_1F_2S_1$ display more balanced or average values of hardness and elastic modulus, lying between the values of $P_1G_3F_2S_2$ and $P_1G_3F_1S_2$. The combination of low power (P_1), medium gas flow rate (G_2), and lowest stand-off (S_1) did not help achieve optimum mechanical properties. The low hardness and elastic modulus of $P_1G_2F_1S_1$ and $P_1G_2F_2S_1$ can be attributed to the combination of low density (96.8% and 95.3%) and relatively low amorphous content (42.68% and 44.32%). This

combination of low density and lower amorphous phase could not resist localized load upon indentation and will result in overall lower mechanical properties.

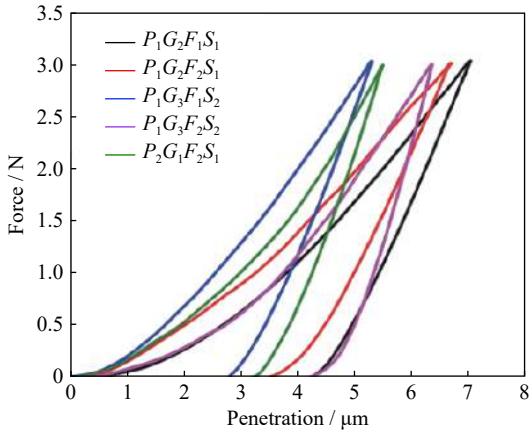

Fig. 5. Load versus depth curve of plasma-sprayed Fe-based coatings during micro-indentation.

Table 4. Hardness and elastic modulus of plasma-sprayed Fe-based coatings

Parameters	Hardness / GPa	Elastic modulus / GPa
$P_1G_2F_1S_1$	4.60 ± 0.43	47.06 ± 3.73
$P_1G_2F_2S_1$	5.17 ± 0.05	47.35 ± 0.35
$P_1G_3F_2S_2$	5.79 ± 0.56	89.65 ± 3.15
$P_2G_1F_2S_1$	6.05 ± 0.05	72.30 ± 1.70
$P_1G_3F_1S_2$	6.56 ± 0.97	67.35 ± 0.45

3.5. Tribological property investigation

Ball-on disk tribometer was used to evaluate the wear property of the coatings. Wear tests were carried out at 250 r/min and at normal loads of 20 N with a stationary sample and rotating ball. Tests were repeated two times to maintain reproducibility. Fig. 6 shows the wear depth versus time graph of the coatings, and the wear depth values after the experiment are tabulated in Table 5. Wear depth was considered the difference between the unworn coating with the maximum depth/crater formed during the experiment. The lowest wear depth was observed for the coating synthesized at $P_1G_3F_1S_2$, while the highest wear depth was observed for $P_1G_2F_2S_1$. The lowest wear depth of $P_1G_3F_1S_2$ could be corroborated to the highest relative density (98.1%) and hardness (6.56 GPa) of the coating, which prevented chipping of the coating material during wear.

Fig. 7 shows the coefficient of friction (COF) versus time graph, and the average COF values are tabulated in Table 5. The coating synthesized at process parameters of $P_1G_3F_1S_2$ shows the lowest COF (0.52 ± 0.04). The lowest COF of this coating could be attributed to the combination of the highest hardness and the higher amorphous content of the coating, which might have prevented excessive brittle fracture during wear [28]. Moreover, the higher hardness and relative density of the coating reduced the formation of debris, which initiated third-body wear during the process [29]. The value of

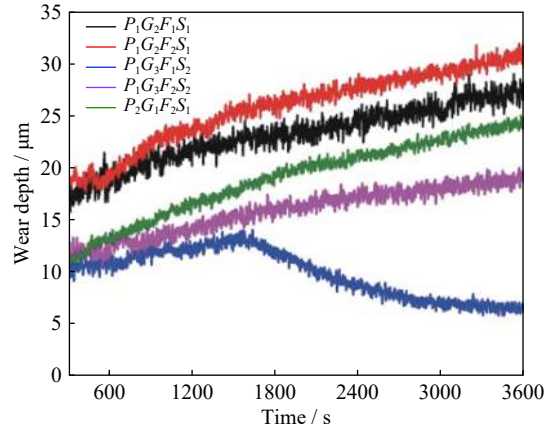

Fig. 6. Wear depth versus time graph of plasma-sprayed coating synthesized at five different parameters.

Table 5. COF and wear depth of plasma-sprayed coating synthesized at five different parameters

Parameters	COF	Wear depth / m
$P_1G_2F_1S_1$	0.61 ± 0.06	23.11 ± 2.74
$P_1G_2F_2S_1$	0.69 ± 0.05	25.70 ± 3.54
$P_1G_3F_1S_2$	0.52 ± 0.04	9.89 ± 2.26
$P_1G_3F_2S_2$	0.64 ± 0.06	15.84 ± 2.24
$P_2G_1F_2S_1$	0.67 ± 0.03	18.95 ± 3.69

wear depth for $P_1G_3F_1S_2$ starts to decrease after ~1700 s of wear, which could be attributed to subsequent smoothening of the surface pores present in the coating and the adherence of the debris particulates on the worn surface at the point of contact of the ball and the coating surface. Moreover, the curve remained the lowest throughout the entire wear experiment, proving that the coating has higher wear resistance than the other samples. The remaining coatings display almost a similar COF, with $P_1G_2F_2S_1$ displaying the highest COF of (0.69 ± 0.05) and the highest wear depth. This result could be due to the combination of relatively low density, hardness, and elastic modulus of the coating, which resulted in easy removal of debris, thereby giving rise to excessive third-body wear. This condition in turn results in the highest wear depth and COF among all the coatings.

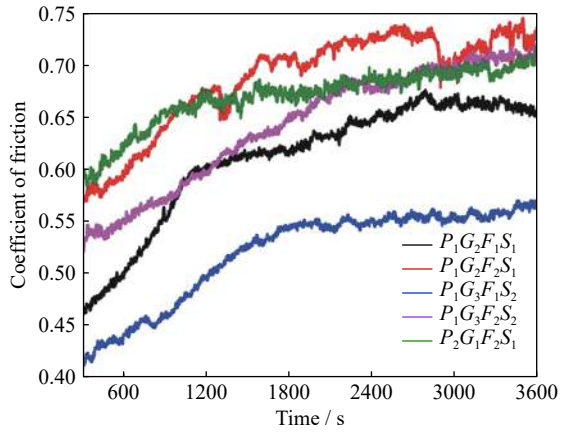

Fig. 7. COF versus time graph of plasma-sprayed coating synthesized at five different parameters.

3.6. Corrosion behavior

Fig. 8 shows the potentiodynamic polarization curves of all the five coatings, and the values are tabulated in Table 6. The potentiodynamic polarization test of the samples was maintained between −0.9 to 0.1 V. Thus, a less passive region was obtained for all samples. As the corrosion current density, i_{corr} is a measure of the extent of electron transfer between the corrosion medium and the sample, it indirectly provides the corrosion resistance of the samples. Table 6 shows that $P_2G_1F_2S_1$ has the least corrosion current density, whereas other samples displayed comparatively higher values. Therefore, the $P_2G_1F_2S_1$ sample is the most corrosion resistant among all samples. The difference between the corrosion rates of all other coatings is marginal. With reference to all the previous studies, all the coatings can be said to have good corrosion resistance in 3.5wt% NaCl aqueous environment because the corrosion rates are reported to be lower than 0.127 mm/a as compared with crystalline iron, whose corrosion rate is in the range of 0.305–0.381 mm/a [30]. The presence of amorphous phase, combined with high density (>95%) of the coatings, helps inhibit corrosion by not allowing corrosive media to reach the substrate. In addition, for all the samples, Si can be anticipated to diffuse upward and form a passive SiO_2 film on the surface, promoting similar corrosion resistance of the coatings [31].

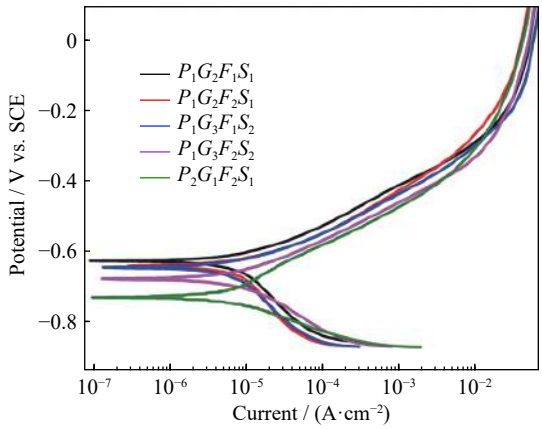

Fig. 8. Tafel plot of plasma-sprayed coating synthesized at five different parameters.

Table 6. I_{corr}, E_{corr}, and corrosion rate of coatings synthesized at five different parameters

Parameters	i_{corr} / (μA·cm^{-2})	Corrosion rate / (mm·a^{-1})	E_{corr} / mV
$P_2G_1F_2S_1$	4.720	0.055	−728.0
$P_1G_3F_1S_2$	7.030	0.082	−644.0
$P_1G_3F_2S_2$	7.820	0.091	−677.0
$P_1G_2F_1S_1$	8.560	0.099	−626.0
$P_1G_2F_2S_1$	8.740	0.101	−640.0

4. Conclusion

In this study, the fabrication process of the Fe-based amorphous/crystalline coating by plasma spraying is optimized by varying four key parameters. Post-coating results confirmed the increase in amorphous phase content in all the coatings as compared with the feed stock powder. A higher plasma power (35 kW) led to excessive melting and subsequent burning of the coatings. The amorphous phase content in the coating decreased with higher power. The increase in gas flow rate also demonstrated a positive impact on the amorphous phase content in the coating. Furthermore, a higher stand-off distance showed higher amorphous phase formation, and vice versa. Moreover, all coatings displayed a density higher than 94%. However, the coatings fabricated using the lowest power, highest gas flow rate, and larger stand-off distance displayed the highest density and improved mechanical and wear properties. Furthermore, all the coatings displayed good corrosion resistance in a 3.5wt% NaCl aqueous environment, with corrosion rates varying between 0.05–0.11 mm/a.

Acknowledgements

The authors sincerely acknowledge the financial support provided by Tata Steel Limited, Jamshedpur, India. The authors also sincerely acknowledge the support from the Indian Institute of Technology Patna.

Conflict of Interest

The authors declare no potential conflict of interest.

Supplementary Information

The online version contains supplementary material available at https://doi.org/10.1007/s12613-020-2171-4

Additional file 1: Table S1. Average temperature and velocity of the Fe based powder particle measured at several different parameters during the Accuraspray experiment. **Table S2.** Flowability of the Alloy-1 powder by keeping the theoretical feed rate as 4 g/min, carrier gas pressure 414 kPa and carrier gas flow as 0.28 m^3/h and vibrator air pressure as 138 kPa. **Table S3**. DSC of Fe based alloys free standing Coatings depicting the enthalpy of crystallization (ΔH) of all the five coatings. **Fig. S1**. DSC isotherm of the Fe based powder. **Fig. S2**. Digital image of the coatings fabricated using (a) P_3 = 35 kW showing melted coatings and (b) $P_2G_3F_1S_1$ also showing sign of melting. **Fig. S3**. DSC isotherm for the Fe based coatings synthesized at parameters set (a) $P_1G_3F_2S_2$; (b) $P_1G_2F_1S_1$; (c) $P_2G_1F_2S_1$; (d) $P_1G_3F_1S_2$; (e) $P_1G_2F_2S_1$. **Section S1.** Test of the powder flowability.

References

[1] A.L. Greer, Metallic glasses, *Science*, 267(1995), No. 5206, p. 1947.
[2] M.F. Ashby and A.L. Greer, Metallic glasses as structural materials, *Scripta Mater.*, 54(2006), No. 3, p. 321.
[3] D.B. Miracle, A structural model for metallic glasses, *Nat. Mater.*, 3(2004), No. 10, p. 697.
[4] V. Ponnambalam, S.J. Poon, G.J. Shiflet, V.M. Keppens, R.

Taylor, and G. Petculescu, Synthesis of iron-based bulk metallic glasses as nonferromagnetic amorphous steel alloys, *Appl. Phys. Lett.*, 83(2003), No. 6, p. 1131.
[5] C. Suryanarayana and A. Inoue, Iron-based bulk metallic glasses, *Int. Mater. Rev.*, 58(2013), No. 3, p. 131.
[6] X.J. Gu, S.J. Poon, and G.J. Shiflet, Mechanical properties of iron-based bulk metallic glasses, *J. Mater. Res.*, 22(2007), No. 2, p. 344.
[7] B.A. Sun and W.H. Wang, The fracture of bulk metallic glasses, *Prog. Mater. Sci.*, 74(2015), p. 211.
[8] Y.C. Li, C. Zhang, W. Xing, S.F. Guo, and L. Liu, Design of Fe-based bulk metallic glasses with improved wear resistance, *ACS Appl. Mater. Interfaces*, 10(2018), No. 49, p. 43144.
[9] A. Kumar, R. Kumar, P. Bijalwan, M. Dutta, A. Banerjee, and T. Laha, Fe-based amorphous/nanocrystalline composite coating by plasma spraying: Effect of heat input on morphology, phase evolution and mechanical properties, *J. Alloys Compd.*, 771(2019), p. 827.
[10] J. Pan, Q. Chen, N. Li, and L. Liu, Formation of centimeter Fe-based bulk metallic glasses in low vacuum environment, *J. Alloys Compd.*, 463(2008), No. 1-2, p. 246.
[11] Q.J. Chen, S.B. Guo, X.J. Yang, X.L. Zhou, X.Z. Hua, X.H. Zhu, and Z. Duan, Study on corrosion resistance of Fe-based amorphous coating by laser cladding in hydrochloric acid, *Phys. Procedia*, 50(2013), p. 297.
[12] A. Inoue, F.L. Kong, Q.K. Man, B.L. Shen, R.W. Li, and F. Al-Marzouki, Development and applications of Fe- and Co-based bulk glassy alloys and their prospects, *J. Alloys Compd.*, 615(2014), p. S2.
[13] J. Sort, D.C. Ile, A.P. Zhilyaev, A. Concustell, T. Czeppe, M. Stoica, S. Suriñach, J. Eckert, and M.D. Baró, Cold-consolidation of ball-milled Fe-based amorphous ribbons by high pressure torsion, *Scripta Mater.*, 50(2004), No. 9, p. 1221.
[14] J. Shen, Q.J. Chen, J.F. Sun, H.B. Fan, and G. Wang, Exceptionally high glass-forming ability of an FeCoCrMoCBY alloy, *Appl. Phys. Lett.*, 86(2005), No. 15, art. No. 151907.
[15] H.X. Li, Z.C. Lu, S.L. Wang, Y. Wu, and Z.P. Lu, Fe-based bulk metallic glasses: Glass formation, fabrication, properties and applications, *Prog. Mater. Sci.*, 103(2019), p. 235.
[16] Z. Zhou, L. Wang, D.Y. He, F.C. Wang, and Y.B. Liu, Microstructure and electrochemical behavior of Fe-based amorphous metallic coatings fabricated by atmospheric plasma spraying, *J. Therm. Spray Technol.*, 20(2011), No. 1-2, p. 344.
[17] S. Kumar, J. Kim, H. Kim, and C. Lee, Phase dependence of Fe-based bulk metallic glasses on properties of thermal spray coatings, *J. Alloys Compd.*, 475(2009), No. 1-2, p. L9.
[18] C. Zhang, L. Liu, K.C. Chan, Q. Chen, and C.Y. Tang, Wear behavior of HVOF-sprayed Fe-based amorphous coatings, *Intermetallics*, 29(2012), p. 80.
[19] P. Fauchais, Understanding plasma spraying, *J. Phys. D: Appl. Phys.*, 37(2004), No. 9, p. R86.
[20] R.Q. Guo, C. Zhang, Q. Chen, Y. Yang, N. Li, and L. Liu, Study of structure and corrosion resistance of Fe-based amorphous coatings prepared by HVAF and HVOF, *Corros. Sci.*, 53(2011), No. 7, p. 2351.
[21] G.Y. Koga, R. Schulz, S. Savoie, A.R.C. Nascimento, Y. Drolet, C. Bolfarini, C.S. Kiminami, and W.J. Botta, Microstructure and wear behavior of Fe-based amorphous HVOF coatings produced from commercial precursors, *Surf. Coat. Technol.*, 309(2017), p. 938.
[22] C.Y. Zhang, Z.H. Chu, F.S. Wei, W.J. Qin, Y. Yang, Y.C. Dong, D. Huang, and L. Wang, Optimizing process and the properties of the sprayed Fe-based metallic glassy coating by plasma spraying, *Surf. Coat. Technol.*, 319(2017), p. 1.
[23] Y.Z. Xing, Z. Liu, G. Wang, X.H. Li, C.P. Jiang, Y.N. Chen, Y. Zhang, X.D. Song, and M. Dargusch, Improvement of interfacial bonding between plasma-sprayed cast iron splat and aluminum substrate through preheating substrate, *Surf. Coat. Technol.*, 316(2017), p. 190.
[24] P. Bijalwan, K.K. Pandey, B. Mukherjee, A. Islam, A. Pathak, M. Dutta, and A.K. Keshri, Tailoring the bimodal zone in plasma sprayed CNT reinforced YSZ coating and its impact on mechanical and tribological properties, *Surf. Coat. Technol.*, 377(2019), art. No. 124870.
[25] R.S. Maurya, A. Sahu, and T. Laha, Quantitative phase analysis in $Al_{86}Ni_8Y_6$ bulk glassy alloy synthesized by consolidating mechanically alloyed amorphous powder via spark plasma sintering, *Mater. Des.*, 93(2016), p. 96.
[26] S. Khandanjou, M. Ghoranneviss, and S. Saviz, The investigation of the microstructure behavior of the spray distances and argon gas flow rates effects on the aluminum coating using self-generated atmospheric plasma spray system, *J. Theor. Appl. Phys.*, 11(2017), No. 3, p. 225.
[27] A.R.M. Sahab, N.H. Saad, S. Kasolang, and J. Saedon, Impact of plasma spray variables parameters on mechanical and wear behaviour of plasma sprayed Al_2O_3 3%wt TiO_2 coating in abrasion and erosion application, *Procedia Eng.*, 41(2012), p. 1689.
[28] M.A. Moore and F.S. King, Abrasive wear of brittle solids, *Wear*, 60(1980), No. 1, p. 123.
[29] S. Ranjan, B. Mukherjee, A. Islam, K.K. Pandey, R. Gupta, and A.K. Keshri, Microstructure, mechanical and high temperature tribological behaviour of graphene nanoplatelets reinforced plasma sprayed titanium nitride coating, *J. Eur. Ceram. Soc.*, 40(2020), No. 3, p. 660.
[30] M.G. Fontana, *Corrosion Engineering*, 3rd ed., McGraw Hill Book Co, New York, 1986.
[31] C.A.C. Souza, D.V. Ribeiro, and C.S. Kiminami, Corrosion resistance of Fe–Cr-based amorphous alloys: An overview, *J. Non Cryst. Solids*, 442(2016), p. 56.